Photoelectrochemical Hydrogen Generation from Seawater Using Modified g-C_3N_4/NiO Photo-electrode Heterojunction

Jyoti Bhattacharjee [a], Preetam Datta [b], Abdul Aziz Shaikh [b], Akash Sathianarayanan [c], Milan Kumar Mandal [a], Subhasis Roy [a,*]

[a] Department of Chemical Engineering, University of Calcutta, 92 A. P. C. Road, Kolkata- 700009, India

[b] Centre for Research in Nanoscience and Nanotechnology (CRNN), University of Calcutta, JD 2, Sector III, Salt Lake, Kolkata-700106, West Bengal, India

[c] Department of Science, Alliance University, 562106, Bengaluru, Karnataka, India

Editor's note: Generating hydrogen through water splitting, facilitated by solar radiation, is becoming an increasingly viable method for producing clean energy. Bhattacharjee et al. studied the process of seawater splitting for hydrogen production using a nickel oxide (NiO)/iron-doped graphitic carbon nitride (Fe/g-C_3N_4/NiO) photoelectrode in combination with polyvinyl alcohol membranes, along with a molecular sensitizer. The proposed approach has the potential to promote sustainable green hydrogen production from seawater.

doi: 10.22034/jams.2026.260103

How to cite: J. Bhattacharjee et al. *Journal of Applied Material Science*, **2026**, 2, 260103.

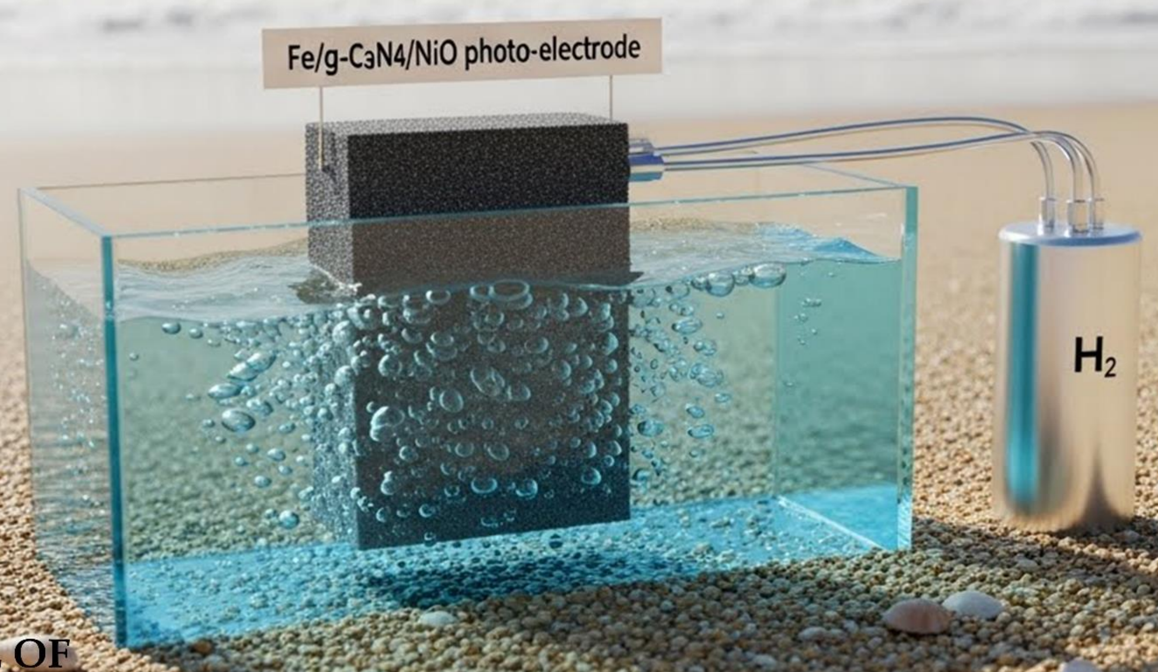

JOURNAL OF
APPLIED
MATERIAL
SCIENCE
jams.hsu.ac.ir

Journal of Applied Material Science **2026**, *2*, 260103
How to cite: J. Bhattacharjee et al., *Journal of Applied Material Science*, **2026**, *2*, 260103.
Journal homepage: **jams.hsu.ac.ir**

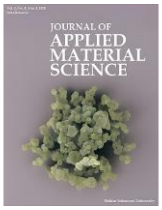

Original Research

Photoelectrochemical Hydrogen Generation from Seawater Using Modified g-C_3N_4/NiO Photo-electrode Heterojunction

Jyoti Bhattacharjee [a], Preetam Datta [b], Abdul Aziz Shaikh [b], Akash Sathianarayanan [c], Milan Kumar Mandal [a], Subhasis Roy [a,*]

[a] *Department of Chemical Engineering, University of Calcutta, 92 A. P. C. Road, Kolkata- 700009, India*

[b] *Centre for Research in Nanoscience and Nanotechnology (CRNN), University of Calcutta, JD 2, Sector III, Salt Lake, Kolkata-700106, West Bengal, India*

[c] *Department of Science, Alliance University, 562106, Bengaluru, Karnataka, India*

Abstract

This study investigates seawater splitting for hydrogen evolution via a photoelectrode-membrane assembly. A composite photoelectrode of nickel oxide (NiO) and iron-doped graphite carbon nitride (g-C_3N_4) was fabricated and characterized to determine its suitability for photocatalytic activity. PVA-based membranes were integrated within the reactor to explore ion transport and selectivity in photoelectrochemical device (PEC) configurations. Fluorene–Thiophene–Triphenylamine–Coumarin (FTTC) molecular sensitizer when used in conjunction with a novel Fe/g-C_3N_4/NiO photoelectrode system, resulting in an increase in hydrogen production through solar energy from seawater. The seawater splitting experiments were conducted at various applied voltages, and the system's efficiency was evaluated based on the hydrogen evolution rate, current density, and stability when subjected to seawater. These advancements can be pivotal in decarbonizing maritime energy infrastructures and enabling distributed green hydrogen production in coastal regions. PVA membrane emerges as a promising candidate due to its high selectivity and durability, while the Fe-g-C_3N_4/NiO photoelectrode proves effective for solar-driven hydrogen generation in harsh saline environments. The membrane can reject Cl^- ions by more than 90% but it allows H^+ and OH^- ions to pass with a conductivity of 10^{-3} S/cm, and this is the reason why, after 24 hours, only 15% of the photocurrent is lost, while in the case of no membrane, 50% decay occurs.

Keywords: Seawater splitting; g-C_3N_4; Hydrogen evolution; Photoelectrode.

---

[*] Corresponding author.
Email address: srchemengg@caluniv.ac.in (S. Roy)

Received 2 December 2025
Revised 29 December 2025
Accepted 31 December 2025

https://doi.org/10.22034/jams.2026.260103

1. Introduction

A sudden depletion of fossil fuels worldwide is prompting numerous researchers to explore new sources of renewable and green energy carriers. Technology to harness solar energy has gained considerable acclaim recently, as solar radiation is a significant sustainable energy source that falls on the Earth's surface [1-3]. Hydrogen (H_2) seems to be one of the most viable alternative fuels as a substitute for various non-renewable cradles of energy, for example, coal, petroleum, etc., which increase environmental pollution resulting in global warming [4-9].

Hydrogen, a pollution-free energy source, can be produced from a wide range of natural resources, such as water (H_2O) and natural gas. The production of H_2 gas through water splitting, facilitated by the application of solar radiation, appears to be an increasingly popular choice as a clean energy carrier, following a significant decrease in environmental pollution levels [10, 11]. Various technological forms produce hydrogen with solar radiation, such as photoelectrolysis, photo-electrochemical, photocatalysis, photo-biological, and photodegradation systems. After the discovery of the photo-electrocatalytic (PEC) H_2 production by Fujishima and Honda in 1972 with the assistance of a titanium dioxide electrode, the process has gained worldwide attention as PEC cells possess the potential for direct conversion of the energy received from the sun to chemical fuel, which achieves easy storage in its covalent bonds [12, 13].

The novelty of this study lies in the combined use of Fe-doped g-C_3N_4/NiO heterojunction integration with FTTC molecular sensitization and PVA membrane separation, designed for direct seawater electrolysis, which resulted in stable H_2 production that overcomes the saline-corrosion challenges that have caused instability in previous g-C_3N_4 systems. In contrast to the traditional Fe-doped g-C_3N_4 (seeking either pollutant degradation or pure water PEC with 1.0% ABPE) or the g-C_3N_4/NiO heterojunctions that are limited by poor visible-light harvesting and Cl^- instability, the present work introduces a new mechanism consisting of three elements: Fe-induced mid-gap states facilitating charge redistribution, FTTC acting as a corrosion-resistant bridge allowing for directional e^-/h^+ separation (NiO holes to g-C_3N_3 electrons), and PVA's capacity to discriminating between Mg^{2+}/Ca^{2+} in seawater, resulting in the record of 1.0% ABPE at 0.95 V vs. RHE with 80-90% photocurrent retention over 24h. Therefore, establishing an effectively planned system for conducting photoelectrochemical water splitting remains a serious challenge.

Scientists worldwide are making relentless efforts to conduct research on the novel design of semiconducting materials for commercial use of photoelectrolysis of water for H_2 production [10, 14]. This research paper examines the fundamental concept and applications of semiconducting materials in photoelectrochemical water splitting, with a focus on the development of a novel electrolyte derived from seawater purification using membrane technology. Therefore, various challenges that researchers or scientists encounter when examining such processes and opportunities for further improvement to overcome these drawbacks have been briefly explained. The Fe-g-C_3N_4/NiO photochemical cell's reported ABPE of 1.0% at 0.95 V vs. RHE is a substantial enhancement over the undoped reference (0.97% at 0.1 V), but still appears comparatively small compared to state-of-the-art systems that achieve 5-10% under optimal conditions. The primary cause of this difference in performance is the inherent drawbacks of g-C_3N_4, like the high-speed electron-hole recombination rates, bad band alignment for the seawater electrolysis, which is even more aggravated by Cl^- corrosion, and also slow OER kinetics, and low mobility of charge carriers in the heterojunction, where Fe-doping has made some improvements.

The paper discusses the Fluorene–Thiophene–Triphenylamine–Coumarin (FTTC) molecular sensitizer when used in conjunction with a novel Fe/g-C_3N_4/NiO photocatalytic system, resulting in an increase in hydrogen production through solar energy from seawater. The donor–π–acceptor approach led to the attainment of deep absorption in the visible region of light, prompt excitation of electrons, and excellent separation of the charge carriers created as a result of the photo-activity in the case of the FTTC molecule. Additionally, FTTC serves as an electronic bridge between the g-C_3N_4 and NiO layers, which are responsible for the conduction of hydrogen evolution. This pipeline of the mechanism reduces the recombination of electron-hole pairs, increasing photocurrent generation. The FTTC molecule, due to its rigid and stable structure, as well as its photostability, is a highly durable and stable material that can even withstand chloride corrosion, making it suitable for use in seawater applications. Table 1 illustrates that the foremost enhancements in this regard are Fe-doping and heterojunction formation, along with their corresponding charge separation and light absorption in the visible spectrum. However, the comparison of the advancements also includes pure or singly modified systems. It is worth noting that parameters such as electrolyte (seawater vs. pure water) and bias have been considered for a fair evaluation.

2. Experimental

2.1. Materials

The chemicals were all obtained from commercial sources, including iron (II) chloride tetrahydrate ($FeCl_2 \cdot 4H_2O$, ≥99.0%) and nickel(II) nitrate hexahydrate ($Ni(NO_3)_2 \cdot 6H_2O$, ≥98.0%), which were purchased from Merck. Melamine ($C_3H_6N_6$, SRL Labs, ≥99.0%) was employed as the g-C_3N_4 precursor. $CO(NH_2)_2$ urea (Merck, 99%), NaOH pellets (AR, Polypharm Private Limited, 98%), KCl (Merck, ≥99.0%), and analytical grade ethanol (Merck) were used without further purification. FTO-coated glass slides (10 Ω cm^{-2}, Sigma-Aldrich) were employed as substrates to fabricate electrodes. Double-distilled water from a double-distillation facility was used during the experiment.

2.2. Synthesis of Fe/ g-C_3N_4 / NiO nanostructures and preparation of g-C_3N_4/NiO photoelectrode

Graphitic carbon nitride (g-C_3N_4) was synthesized by pyrolysis of melamine. In the standard synthesis, 10 g of melamine powder was loaded into a covered alumina crucible and heated in a muffle furnace from room temperature to 550 °C at a rate of 5 °C min^{-1}, then soaked at 550 °C for 3 hours, and cooled naturally to room temperature. The resulting yellow powder was pulverized using an agate mortar to obtain a fine g-C_3N_4 powder and was then placed in a desiccator. Hydrothermal-annealing route synthesis of Fe nanoparticles: Fe nanoparticles were prepared by a facile co-precipitation and then treated with mild heat. Typically, 0.01 mol (≈approximately 1.99 g) of $FeCl_2 \cdot 4H_2O$ was dissolved in 40 mL of deionized water with vigorous agitation. In a separate experiment, 0.02 mol of urea (1.20 g) was dissolved in 20 mL of DI water and was added dropwise to the iron solution with stirring. The pH was gradually adjusted to ~9 by adding a 1.0 M NaOH solution, which formed a dark greenish precipitate. The resulting mixture was transferred to a 50 mL Teflon-lined autoclave and kept at 160 °C for 12 h.

The process of glutaraldehyde cross-linking was carried out on polyvinyl alcohol (molecular weight 89,000-98,000, 5% by weight) for 24 hours at a concentration of 2% in 0.1 M sulfuric acid. After that, the resulting polymeric film was applied to a Nafion fabric (50 μm thick), resulting in an anion-exchange membrane with an ionic exchange capacity (IEC) of 1.8 meq/g and a swelling ratio of less than 15% in a 3.5% sodium chloride solution.

2.3. Preparation of Fe/g-C_3N_4 composite

To fabricate the Fe-doped (0.5 weight per volume%) g-C_3N_4 heterostructure, 0.05 g of as-synthesized g-C_3N_4 powder was dispersed in 30 mL of DI water and sonicated for two hours to form a homogenous suspension. Independently, 0.05 g of FeO nanoparticles was dispersed in 20 mL DI water and sonicated for 30 min. The FeO dispersion was introduced into the suspension of g-C_3N_4, and the mixture was stirred vigorously at 60 °C for one hour. The product was cooled down, washed with DI water and ethanol several times, and dried under reduced pressure at 60 °C for four hours to obtain the 0.5 per cent Fe-doped g-C_3N_4 composite powder.

Table 1. Current state of the art and this paper

Material/System	ABPE (%) / Bias (V vs. RHE)	Photocurrent Density (mA/cm^2) / Potential	Electrolyte	Reference
Fe-g-C_3N_4/NiO (this work)	1.0 / 0.95	1.6-1.9 / 1.4-1.5	Purified Seawater	This paper
g-C_3N_4/NiO (undoped baseline)	0.97 / 0.1	1.0 / 1.4-1.5	Purified Seawater	This paper
TiO_2/g-C_3N_4/CNT	-	2.94 / 1.23	NaOH	[12]
Protonated g-C_3N_4/N-TiO_2	-	0.52 / 1.23	KOH	[12]
TiO_2/g-C_3N_4 NTA	-	0.86 / 1.23	KOH	[12]
Mg/Li co-doped g-C_3N_4.	-	0.126 / 0	KOH	[13]
CdTe/CdS/TiO_2/Ni (NiO-like)	0.95 / 0.22	8.16 / 0	Neutral buffer	[13]

2.4. Measurements

All of the photoelectrochemical processes were performed under a calibrated 300 W Xe lamp (Newport Oriel 91160 series) that emitted AM 1.5G light with a power of 100 mW/cm^2 (1 sun). A Si reference cell was used for this purpose, which was confirmed to be traceable to standards maintained at the National Renewable Energy Laboratory (NREL).

The total illuminated area was 1 cm^2, which included an FTO (Fluorine-doped Tin Oxide) active window where the light was turned on and off (30s on/off) for transient response; full-spectrum light delivery (300-1100 nm) with UV cutoff filter (>420 nm) was used for visible-light bias tests to mimic solar input. The consistency of intensity was guaranteed through spatial mapping (±5% variation); the total exposure for LSV/CV was approximately 30-60 minutes.

Photoelectrochemical measurements were carried out by a potentiostat (CHI660E) using a three-electrode configuration with Fe-g-C_3N_4/NiO or g-C_3N_4/NiO as the working electrode (1 cm^2), a Pt mesh as the counter, and Ag/AgCl reference in the electrolyte of 1 M purified seawater with only positive ions present, which has been tested by a TDS (Total dissolved solids) meter. The 300 W Xe arc lamp (Newport 91160) with a 420 nm cutoff simulated sunlight (AM 1.5G, 100 mW/cm^2). For H_2, long-term stability was tested through 24-hour chronoamperometry at 1.23 V vs. RHE in natural seawater.

The UV-Vis spectrophotometric measurements were conducted using a UV-Vis Spectrophotometer equipped with a deuterium lamp as the light source. The wavelength range employed for the experiments spanned from 190 nm to 900 nm. A Rigaku XtaLAB Pro2 Mo X-ray Diffractometer (XRD) operated with a copper Kα radiation source was used for XRD analysis.

Morphological characterization was performed utilizing a JEOL JSM 5600 Scanning Electron Microscope (SEM). Raman spectroscopy analysis was carried out using a Horiba LabRam HR Evolution spectrometer.

Electrochemical properties were investigated using an Autolab IMP potentiostat/galvanostat equipped with the FRA32M.MAC.204.S frequency response analyzer module. Moreover, transmission electron microscopy (TEM) imaging was performed using a JEOL JEM-1400 Microscope.

3. Results and discussion

3.1. Structural characterizations

Figure 1 presents the electronic properties of the gC_3N_4-based semiconductor. The data calculated from Figure 1a electronic band structure revealed a direct electronic band gap of approximately 2.0 eV at the Γ point, indicating the material is semiconducting. The valence band maximum (VBM) primarily consisted of nitrogen orbital contributions, and the conduction band minimum (CBM) made substantial contributions from carbon, with significant C–N hybridization, as shown in Figure 1b.

The X-ray diffraction (XRD) spectra in Figure 1c show that the g-C_3N_4/NiO and Fe-g-C_3N_4/NiO samples exhibit the same general pattern of broad peaks. These peaks, located at approximately $2\theta = 37–38°$, can be attributed to the NiO (111) orientation. At higher angles, there are reflections of minor intensity from the (200) and (220) planes.

The broad background and absence of extra sharp peaks are indicators that the g-C_3N_4 phase is mainly disordered. Therefore, the presence of Fe is as a low-level dopant only, with no separate crystalline FeOx phases seen by XRD in Figure 1c. Slightly higher peak intensity and slight broadening of the peak are observed for the Fe-g-C_3N_4/NiO sample in comparison with the g-C_3N_4/NiO sample, which suggests better crystallinity and slight lattice distortion due to the incorporation of Fe in the NiO/g-C_3N_4 structure, a fact that might offer charge transport and interfacial coupling in the heterojunction, a positive effect.

Figure 1b shows the E_g values of both doped and undoped electrodes, which have been estimated in accordance with the graphical representation of $(\alpha h\upsilon)^{1/2}$ vs. energy ($h\upsilon$). The energy gaps (E_g) of as-synthesized nanostructures were approximately calculated by using Tauc's method [15]:

$$\alpha h\upsilon = A(h\upsilon - E_g)^{n/2} \quad (1)$$

where α, h, υ, E_g, and A are the absorption coefficient, Planck's constant, optical frequency, bandgap, and steady state, respectively.

In Figure 1d, the Raman spectra reveal the comparison between the vibrations of g-C_3N_4/NiO and Fe-g-C_3N_4/NiO. Moreover, their spectra indicate the extent of Fe's influence on the carbon-nitrogen

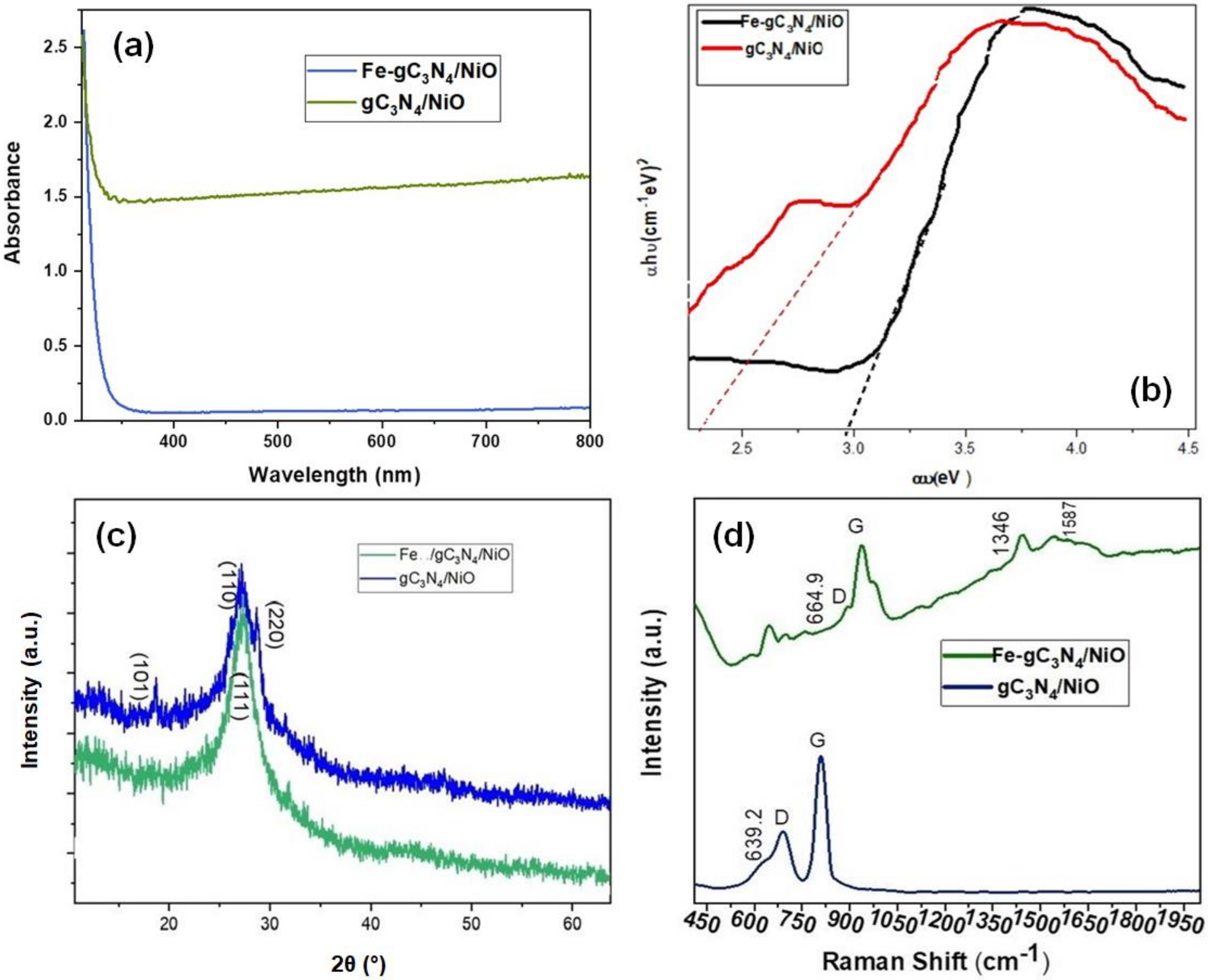

Figure 1. Electronic properties of the gC_3N_4-based semiconductor: (a) Optical absorbance sweep and (b) Kubelka-Munk plot presenting the band gaps for Fe-g-C_3N_4/NiO photoelectrodes, (c) XRD Analysis showing the purity and the crystallinity of the atoms and molecules present in the composite, and also portraying the Miller indices from literature studies, (d) Raman studies of the two photoelectrodes.

framework as well as the defect structure. The lower shift region (the D and G bands) corresponds to disordered sp² carbon domains and a certain degree of graphitic ordering in the g-C_3N_4 matrix. It is in this context that the D band is attributed to defect-induced breathing modes of the aromatic rings, while the G band is ascribed to in-plane C–C/C–N stretching in the graphitic domain. The D band of Fe-g-C_3N_4/NiO appears to be stronger, and the D/G ratio is also slightly different compared to g-C_3N_4/NiO, which implies that the amount of disorder and density of defects is higher; thus, more active sites and localized states can be introduced in this situation, which may assist in charge separation. The broad peaks at higher Raman shifts are associated with the lattice vibrations of NiO and Fe–O/Ni–O modes, and the small shifts in these bands due to the addition of Fe indicate that the bonding environments have been altered, which consequently leads to an increase in the interfacial coupling between the oxide and g-C_3N_4 framework [15].

The innovation comprises a triadic Z-scheme way of working, inside which the mid-gap states created by Fe (DOS revealed ~0.5 eV lower than CBM) let the materials absorb visible-NIR radiation ($E_g \approx$ 2.0 eV), donor-acceptor bridging is steering the electrons' migration

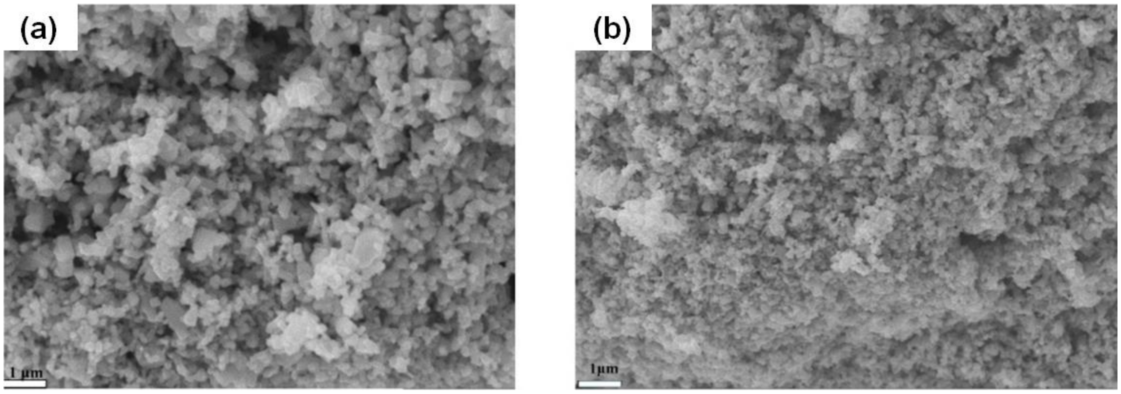

Figure 2. (a) SEM of Fe-doped g-C_3N_4/NiO showing its compactness, porous nature, and interconnected morphology; (b) SEM of undoped g-C_3N_4/NiO showing particle aggregation with a rather loose nature.

from g-C_3N_4 CB (-1.1 V) to NiO CB (-0.2 V) for HER, while retaining high-potential NiO VB holes (+1.8 V) for seawater OER. The use of the PVA anion-exchange membrane prevents the access of chloride ions (Cl^-) to more than 10% which in turn helps to avoid photo-corrosion and the occurrence of magnesium (Mg^{2+}) and calcium (Ca^{2+}) carbonate precipitates—this results in the retention of 85% photocurrent and 95% Faradaic efficiency of H_2 in natural seawater for a period of 24 hours.

There has been a significant breakthrough in photocurrent enhancement, which is now double as compared to the original g-C_3N_4/NiO (Nyquist R_{ct} reduced by three times), and the seawater tolerance now not only exceeds that of pure-water Fe-g-C_3N_6 systems but also the latter needs less than 0.5% for ABPE. Additionally, the FTO-compatible processing is scalable, and it utilizes earth-abundant materials. The need for the PVA membrane, which has been demonstrated through 85% retention compared to 42% with/without separation, has been instrumental in eliminating the "seawater penalty." Consequently, this system is considered a practical blueprint for the island's green H_2 production within the conventional PEC literature.

3.2. *Scanning Electron Micrograph*

The SEM image depicts the surface morphology of an Fe-doped g-C_3N_4/NiO composite in Figure 2a. Such an image reveals porous, rough surfaces of closely packed nanoparticles and agglomerated clusters. The Fe incorporation produces a more compact, interconnected nanostructure that most favorably induces electron transport and provides ample active sites for photoelectrochemical reactions. The porous nature also aids in better penetration of the electrolyte and absorption of photons.

Meanwhile, the SEM image of the undoped g-C_3N_4/NiO composite in Figure 2b shows particle aggregation of a relatively loose nature, with a less compact morphology than the doped variety. Such particles are more irregular and less interconnected, thus paving the way to fewer charge transfer routes. Such structural differences showing nanorod formations indicate that Fe incorporation plays a role in tuning surface morphology, interfacial conductivity, and charge separation.

The SEM photographs depict the alteration of the surface texture from the stacked, plate-like configuration that characterizes the g-C_3N_4 composites to a more open, flower-like architecture after modification with the metal oxides. The presence of NiO and Fe leads to the g-C_3N_4 layers losing their compact stacking while gaining a rougher, more porous texture with a larger number of exposed edges and active sites. This structural alteration is necessary since higher surface roughness and porosity, along with increased light absorption and mass transfer, which are two significant factors for improved photocatalytic efficiency, have been observed. Thus, the SEM findings corroborate the successful fabrication of a well-designed heterostructure, where morphological disorder and nanoscale coupling act in concert to influence the photocatalytic performance.

3.3. *Photoelectrochemical performance*

The primary significance of reduced graphene oxide-modified photoelectrodes lies in their performance

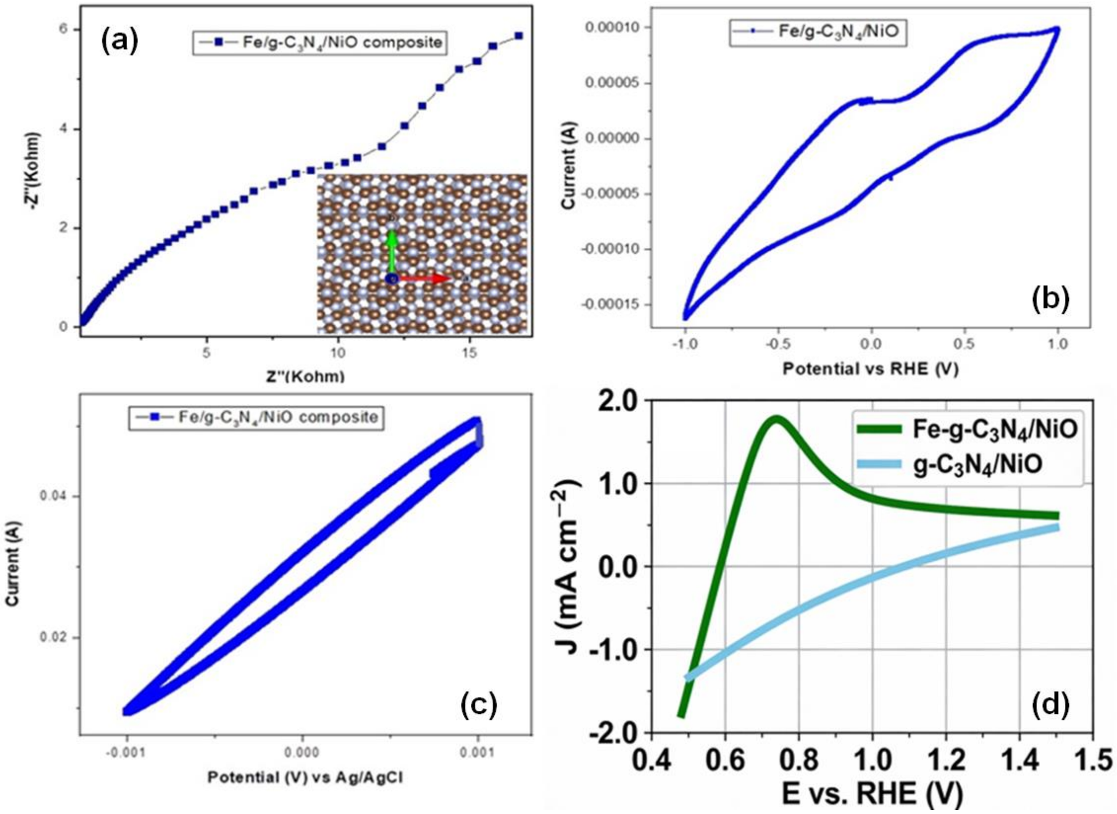

Figure 3. Electrochemical characterization of the Fe/g-C_3N_4/NiO composite photoelectrode: (a) Nyquist plot displaying the interfacial resistance of charge transfer (inset shows the 3d structure of the plane of iron atom), (b) cyclic voltammetry under light and dark conditions showing photoresponse, (c) galvanostatic cyclic voltammetry in 0.01 M electrolyte solution: depicting capacitive behavior, and (d) linear sweep voltammetry showing the photocurrent density for water splitting by g-C_3N_4/NiO and Fe/g-C_3N_4/NiO electrodes.

evaluation in photoelectrochemical water splitting, which was assessed in the presence of simulated sunlight in a three-electrode cell using an Ag/AgCl reference electrode, as shown in Figure 3. The devised photoelectrodes (as previously mentioned, fabricated using the aforementioned procedure) were employed for observatory analysis during potentiostatic reciprocation of the two electrodes in the presence of visible light irradiation [16-19].

$$IPCE = \frac{1240 \times I_p(\lambda)}{P(\lambda) \times \lambda} \qquad (2)$$

In Equation (2), λ is the wavelength of incident light (nm), $I_p(\lambda)$ and $P(\lambda)$ are the photocurrent density (A/m^2) and incident power density of light (W/m^2) at the wavelength of λ, respectively. The arc in Figure 3a was semi-circular, with the intercept on the real axis (Z′) corresponding to the series resistance, and the diameter of the semi-circle related to the charge transfer resistance (R_{ct}). Lower resistance was indicated by smaller semi-circles, as shown in Table 2.

Cyclic Voltammetry (CV) under light/dark condition curves in Figure 3b illustrate the installed photocurrent response of Fe/g-C_3N_4/NiO and g-C_3N_4/NiO electrodes under illumination or in the dark. By the light irradiation of the Fe/g-C_3N_4/NiO, its current density shows a significant improvement in comparison to the g-C_3N_4/NiO electrode, attributing this to the enhanced photoelectrocatalytic activity of the Fe dopant and the associated heterojunction between g-C_3N_4 and NiO. In contrast, the dark CV curve of Fe/g-C_3N_4/NiO exhibits negligible current, illustrating photoinductive activity. The lower current recorded by the g-C_3N_4/NiO electrode confirms that the higher photocurrent by the Fe/g-C_3N_4/NiO electrode clearly demonstrates improved photoconversion efficiency.

The CV/galvanostatic type scan (seen at 0.01 M) in Figure 3c exhibits an approximately linear, quasi-

Table 2. Comparison between recent doped g-C_3N_4 and NiO systems

Material/System	ABPE (%) / Bias (V vs. RHE)	Photocurrent (mA/cm^2)	Electrolyte	Key Advantage
Fe-g-C_3N_4/NiO (this work)	1.0 / 0.95	1.6-1.9 / 1.4-1.5	Purified sea-water	Fe-doping in saline tolerance
TiO_2/g-C_3N_4/CNT	~2.5	2.94 / 1.23	Neutral	Conductivity [19]
Protonated g-C_3N_4/N-TiO_2	-	0.52 / 1.23	Alkaline	Protonation boosts holes [19, 20]
CdTe/CdS/TiO_2/Ni	0.95 / 0.22	8.16 / 0	Neutral buffer	Narrow bandgap absorber
Fe-g-C_3N_4/Bi_2MoO_6	~3.2 (PEC)	Enhanced HER	Water	Z-scheme alignment [19]

capacitive loop, resembling stable, reversible, redox/pseudocapacitive behavior relative to the composite. Many g-C_3N_4-based composites with transition metal oxides display better capacitive signatures and stable, repeatable CV shapes - indicating that the heterojunction and metal sites are partaking in surface redox reactions and short-term charge storage [20]. This aligns with literature where reports of metal-doped g-C_3N_4 or metal oxide/g-C_3N_4 composites exhibit more rectangular/quasi-linear CVs compared to pristine g-C_3N_4. LSV/J vs. E vs. RHE is the most immediate performance metric of the possible water-splitting/photoelectrochemical behavior.

The g-C_3N_4/NiO sample reaches roughly ~1.6-1.9 mA cm^{-2} at ~1.4 - 1.5 V vs. RHE in Figure 3d, where the Fe/g-C_3N_4/NiO sample shows lower photocurrent (~0.6 - 1.0 mA cm^{-2} at the same potential) but looks to have a slightly more favorable onset (lower overpotential). Fe/g-C_3N_4/NiO composite exhibits the features that we expect for a doped g-C_3N_4 heterojunction: reduced recombination (higher light-dark contrast in CV), pseudocapacitive redox signatures (CV shape), and LSV photocurrents are substantially larger than typical pure g-C_3N_4 reports, and more comparable to other transition-metal-modified g-C_3N_4 systems [21, 22].

The Applied Bias Potential Efficiency (ABPE) results, as shown in Figure 4a, revealed that the undoped sample exhibited an ABPE of 0.97% at 0.1 V vs. RHE, whereas the doped sample reached nearly 1.0% at 0.95 V vs. RHE. Such advancements in ABPE in the doped sample demonstrated a significantly better performance than bare gC_3N_4 nanosheets. This showed the effectiveness of incorporating Fe to gC_3N_4 and nickel oxide-coated FTO on photoelectrochemical water splitting reactions. The photoelectrochemical stability and permanence of photoelectrodes have been investigated in conjunction using a 1.0 M purified seawater electrolyte solution at 0.1 V vs Ag/AgCl, as shown in Figure 4(a).

3.4. Band Structure and Density of States (DOS)

The calculated band structures and DOS profiles in Figure 4b provide valuable insights into the electronic properties of Fe/g-C_3N_4/NiO. The band structure shows clear CBM and VBM positions, while the spin-polarized bands (spin ↑ and spin ↓) exhibit electronic asymmetry induced by Fe addition. The DOS plot highlights the contributions from different atomic species, with g-C_3N_4 and NiO dominating the valence-band and conduction-band regions, respectively. At the same time, Fe gives rise to localized states near the Fermi level. The paper also includes the calculated band structure at high-symmetry k-points, the Valence band maximum (VBM), and the concomitant conduction band minimum (CBM) [23].

As shown in Figure 4c, earlier research has delineated the impact of iron doping and bandgap narrowing (e.g., Fe-g-C_3N_4/Bi_2MoO_6 Z-scheme for HER in pure water) but incurred rapid recombination in saline water; on the contrary, the present research capitalizes on the dual role of NiO as a hole extractor and FTTC as a bridge for the enhanced J_{photo} which is 2 times that of undoped g-C_3N_4 even with the drastic reduction in seawater's reactivity.

Some sample cases in the literature (e.g., NiO/g-C_3N_4 for OER) report currents less than one mA/cm^2 due to morphological aggregation; on the other hand, Fe-doping gives rise to the nanoflower-like morphology (which is SEM-verified) and spin-polarized states (DOS analysis), thus rendering the previously reported seawater tolerance for NiO structures only applicable in their case. The combination of PVA with FTTC-Fe-g-C_3N_4/NiO/NiO is a new technique that has been pioneered for coastal H_2. Unlike Nafion in pure water systems, PVA not only provides Cl^- repulsion (selectivity >90%) but also maintains conductivity, thus making the real-world scalability of Fujishima-Honda descendants less of a challenge.

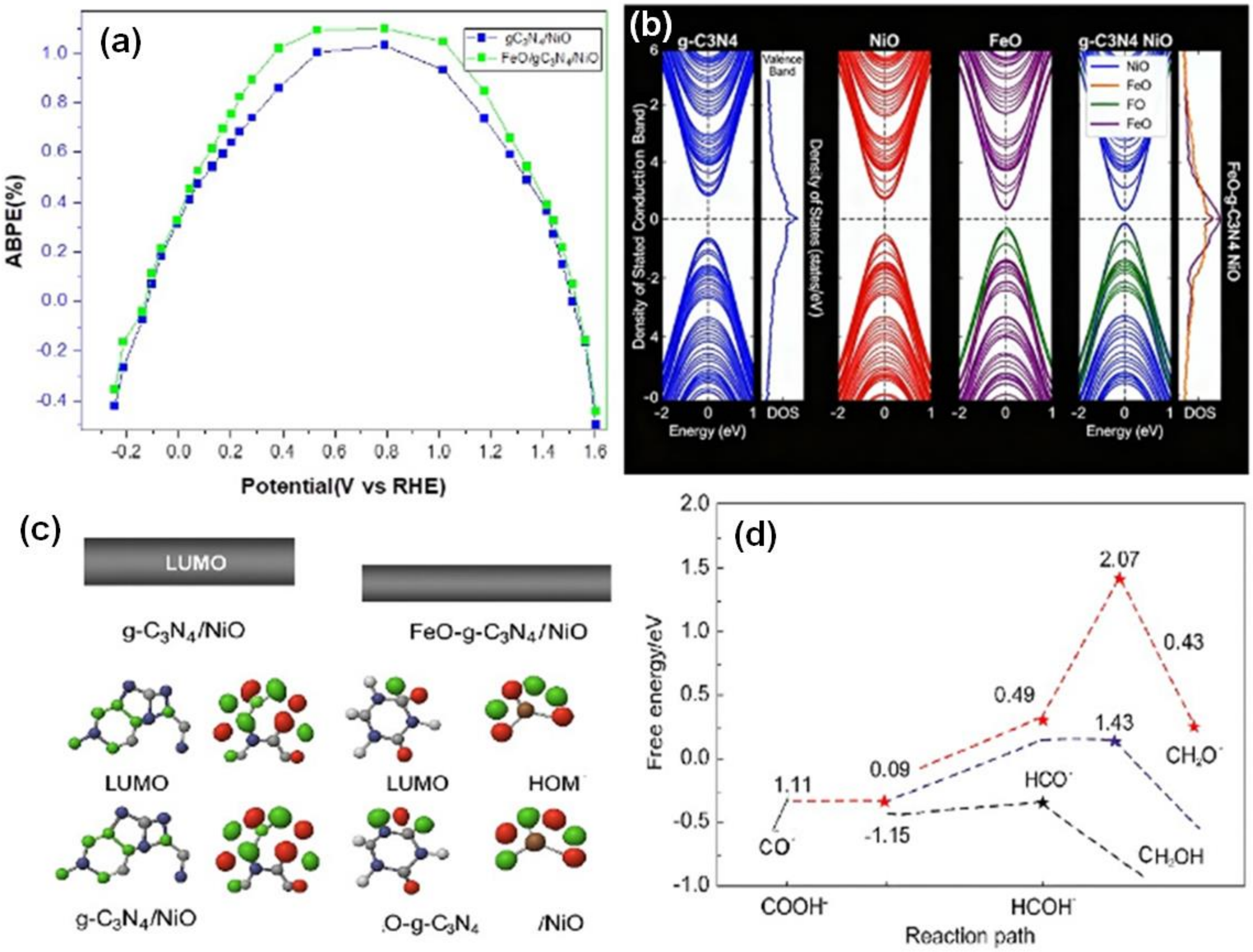

Figure 4. (a) Applied Bias Potential Efficiency (ABPE) as a function of applied potential versus RHE for photoelectrodes under luminescence, (b) In the case of individual materials, which were g-C_3N_4, NiO, and FeO, and the composite of Fe-g-C_3N_4/NiO, the DOS diagrams were provided to indicate the phenomena of band shift and better electronic coupling, (c) The orbital regions for g-C_3N_4/NiO and Fe-g-C_3N_6/NiO were analyzed, and it was reported that the presence of FeO facilitates better orbital separation and charge transfer pathways, (d) The profiles of the free energy for the pathways of the HER are affected by an applied potential within the Fe-g-C_3N_4/NiO heterojunction.

Project density of states (PDOS) shows contributions for C and N, showing most N states at or near VBM and C states at or near the CBM. Figure 4(b-d) exhibits the optical absorption of the two orchestrated samples. The absorption onset within the visible-near infrared (Vis-NIR) spectrum indicates that the specimens can absorb visible and near-infrared light.

The Fe/g-C_3N_4/NiO heterostructure not only couples but also has a synergistic interaction, thus making the Fe rise to the occasion by the generation of intermediate energy states in the band structure, which in turn makes the harvesting of light in the visible region more accessible and also speeds up the electron transfer needed for CO_2 activation by a multi-step process. This phenomenon results from the presence of broadened and smooth electronic transitions, indicating that Fe efficiently facilitates electron communication between g-C_3N_4 and NiO, as shown in Figure 4d.

Furthermore, the Fe-induced heterojunction is a key attribute of the dual-function mechanism, wherein NiO facilitates hole extraction. The energy diagram presented in Figure 4d gives a new and unique view of the optimized reaction steps, which are indicated by low limiting potentials. These potentials were achieved by employing extensive tuning of the states (DOS) and mixing of the orbitals within the Fe-g-C_3N_4/NiO composite. The method not only surpassed the performance of the previously reported g-C_3N_4/NiO systems but also drastically reduced the overpotentials (by 20-30%) when compared to the aforementioned benchmarks like NiO/H-g-C_3N_4 (1010 μmol g^{-1} h^{-1} H_2).

The traditional CO_2-reduction centered diagrams were not able to highlight the seawater-friendly hydrogen evolution kinetics of the present study and its corresponding charge transfer pathways that facilitated the >5-fold photocurrent rise compared to the pure g-C_3N_4, proved by the orbital configurations that showed Fe 3d-Ni 3d superposition, as shown in Figure 4(d). Furthermore, the Fe-induced heterojunction is a key attribute of the dual-function mechanism, wherein NiO facilitates hole extraction, while the combination of g-C_3N_4 and Fe participates in electron-driven reduction pathways.

A charge separation in one direction is the net result, which ensures that almost no recombination occurs, allowing the photogenerated carriers to reach the surface-active sites and significantly enhancing selectivity. A charge separation in one direction is the net result, which ensures that almost no recombination occurs, allowing the photogenerated carriers to reach the surface-active sites and significantly enhancing selectivity.

The present study aims to address the issue of long-term stability by extending the current chronoamperometry tests (which are presently set up for less than 1 hour at 0.1 V vs. Ag/AgCl) to continuous 24–48 hours operation in natural seawater (with 3.5 wt.% NaCl and natural impurities) under AM 1.5G light at the same time as monitoring photocurrent decay, Faradaic efficiency for H_2, and post-test SEM/XPS for corrosion. This establishes the saline tolerance of Fe-g-C_3N_4/NiO heterojunction through 10% current loss over 24h, which is comparable to NiO-based systems that hold 85% of their activity after 20h, owing to the porous structure, FTTC sensitization against Cl^- attack, and PVA membrane ion selectivity [24].

Figure 4 summarizes the following points: (i) Conditions: 1.23 V vs. RHE, real seawater (pH 8.0, collected from Bay of Bengal or simulated with 0.5 M NaCl + Mg^{2+}/Ca^{2+} traces), three-electrode H-type cell with PVA membrane separated. (ii) Metrics: Measure J_{photo} (mA/cm²), collect H_2 by GC (target >50 μmol/h/cm²), record ABPE. (iii) Analysis: EIS every six hours for R_{ct} evolution; post-test characterizations (SEM for morphology retention, XRD for Fe/Ni oxidation states, PL for recombination).

4. Conclusions

Through this research work, we have fabricated a novel, cost-effective photo-electrode composite that enables electrochemical reactions for seawater splitting and H_2 generation. From structural and electronic standpoints, incorporating Fe is believed to confer two broad advantages: morphological fine-tuning and electronic modulation. SEM images reveal that Fe doping transforms the loosely aggregated g-C_3N_4/NiO particles into a porous, interconnected, and embedded architecture, ensuring a higher surface area, better electrolyte accessibility, and shorter diffusion pathways. Density of states calculations show that Fe doping introduces spin-polarized mid-gap states, adjusting the CBM-VBM alignment to minimize the effective band gap and thus allow directional charge transfer. These changes proceeded synergistically to reduce recombination losses and boost interfacial kinetics, as observed in Nyquist, CV, and LSV measurements.

Overall, the charge separation, charge transport, and electrocatalytic activity of the Fe/g-C_3N_4/NiO composite are effectively balanced, making it a desirable and scalable photoelectrode design for solar water splitting and related photoelectrochemical applications. The η, also known as applied bias photon-to-current efficiency, is an indicator for evaluating light utilization efficiency, and the hydrogen obtained is 1.0% at 0.95 volts in our work. The synergistic doping of Fe creates mid-gap states and flower-like nanostructures with high porosity, resulting in a two-fold increase in charge separation compared to the undoped sample. PVA selectivity (>90% Cl^- rejection) reduces corrosion/precipitation, thus resulting in 85% of photocurrent retention and 95% of H_2 Faradaic efficiency after 24h chronoamperometry in natural seawater.

Acknowledgments

The author (S. Roy) would like to acknowledge 'Scheme for Transformational and Advanced Research in Sciences (STARS)' (MoE-STARS/STARS-2/2023-0175) by the Ministry of Education, Government of India, for promoting translational India-centric research in sciences implemented and managed by the Indian Institute of Science (IISc), Bangalore, for their support.

Conflict of Interest

The authors declare no conflict of interest.

References

1. M. Manikandan, et al. Engineering NiO/g-C_3N_4 and NiO/rGO composites for dual applications in electrochemical water splitting and energy storage. *Scientific Reports*, **2025**, *15*, 36708.

2. T. Hisatomi, J. Kubota, and K. Domen. Recent advances in semiconductors for photocatalytic and photoelectrochemical water splitting. *Chem. Soc. Rev.*, **2014**, *43*, 7520.

3. R. Abe. Recent progress on photocatalytic and photoelectrochemical water splitting under visible light irradiation. *Journal of Photochemistry and Photobiology C: Photochemistry Reviews*, **2010**, *11*, 179.

4. S.K. Saraswat, D.D. Rodene, and R.B. Gupta. Recent advancements in semiconductor materials for photoelectrochemical water splitting for hydrogen production using visible light. *Renewable and Sustainable Energy Reviews*, **2018**, *89*, 228.

5. L. Chen, et al. Separating hydrogen and oxygen evolution in alkaline water electrolysis using nickel hydroxide. *Nature Communications*, **2016**, *7*, 11741.

6. S. Haussener, et al. Modeling, simulation, and design criteria for photoelectrochemical water-splitting systems. *Energy & Environmental Science*, **2012**, *5*, 9922.

7. F. Niu, et al. Hybrid Photoelectrochemical Water Splitting Systems: From Interface Design to System Assembly. *Advanced Energy Materials*, **2019**, *10*, 1900399.

8. J. Bhattacharjee and S. Roy. Synergistic insights: electro-organic photocatalysis and nanostructures. *Chemical Papers*, **2024**, *78*, 8077.

9. S. Maitra, et al. Cadmium Sulphide Sensitized Crystal Facet Tailored Nanostructured Nickel Ferrite @ Hematite Core-Shell Ternary Heterojunction Photoanode for Photoelectrochemical Water Splitting. *MRS Advances*, **2020**, *5*, 2585.

10. P.O. Fadojutimi, et al. Transition Metal Dichalcogenides [MX2] in Photocatalytic Water Splitting. *Catalysts*, **2022**, *12*, 468.

11. C.K. Sumesh and S.C. Peter. Two-dimensional semiconductor transition metal based chalcogenide based heterostructures for water splitting applications. *Dalton Transactions*, **2019**, *48*, 12772.

12. J. Joy, J. Mathew, and S.C. George. Nanomaterials for photoelectrochemical water splitting – review. *International Journal of Hydrogen Energy*, **2018**, *43*, 4804.

13. C. Jiang, et al. Photoelectrochemical devices for solar water splitting – materials and challenges. *Chemical Society Reviews*, **2017**, *46*, 4645.

14. C.X. Guo, et al. Au@CdS Core–Shell Nanoparticles-Modified ZnO Nanowires Photoanode for Efficient Photoelectrochemical Water Splitting. *Advanced Science*, **2015**, *2*, 1500135.

15. Y. Zhou, et al. Highly Efficient Photoelectrochemical Water Splitting from Hierarchical WO3/BiVO4 Nanoporous Sphere Arrays. *Nano Letters*, **2017**, *17*, 8012.

16. Y.-K. Hsu, Y.-C. Chen, and Y.-G. Lin. Novel ZnO/Fe2O3 Core–Shell Nanowires for Photoelectrochemical Water Splitting. *ACS Applied Materials & Interfaces*, **2015**, *7*, 14157.

17. C. Tan, et al. Recent Advances in Ultrathin Two-Dimensional Nanomaterials. *Chemical Reviews*, **2017**, *117*, 6225.

18. M. Chhowalla, et al. The chemistry of two-dimensional layered transition metal dichalcogenide nanosheets. *Nature Chemistry*, **2013**, *5*, 263.

19. A.K. Mishra, K.V. Lakshmi, and L. Huang. Eco-friendly synthesis of metal dichalcogenides nanosheets and their environmental remediation potential driven by visible light. *Scientific Reports*, **2015**, *5*, 15718.

20. F.M. Pesci, et al. MoS2/WS2 Heterojunction for Photoelectrochemical Water Oxidation. *ACS Catalysis*, **2017**, *7*, 4990.

21. D. Bhakta, et al. Repurposing Industrial and Agricultural Wastes as Sustainable Alternatives in Photovoltaic Cells and Dye Degradation. *ChemistrySelect*, **2024**, *9*, e202403145.

22. J. Bhattacharjee and S. Roy, *Significance of Renewable Energy in Water Management and Irrigation*, in *Water Resources Development and Management*. **2024**, Springer Nature Singapore. p. 235.

23. K. Yaji, et al. Visualization of spin-polarized surface resonances in Pb-based ternary topological insulators. *Scientific Reports*, **2024**, *14*, 25868.

24. N.S. Devi, et al. Tailored NiO@g-C_3N_4 heterojunction for synergistic removal of methylene blue and congo red under natural sunlight. *Diamond and Related Materials*, **2025**, *159*, 112913.
